Nanoscale, Available online 14 November 2025
DOI: 10.1039/d5nr03432a

Surface Reconstruction of $La_{0.95}Pr_{1.05}CuO_4$ as an Efficient Bifunctional Electrocatalyst for Water Splitting

Amna Altaf [a,b], Manzar Sohail*[a] , K.G.U. Wijayantha[b] , Igor Kraev[c]

[a] Catalysis and Surface Chemistry Laboratory, Department of Chemistry, School of Natural Sciences, National University of Sciences and Technology, Islamabad, 44000, Pakistan.

[b] Centre for Renewable and Low Carbon Energy, School of Water, Energy and Environment, Cranfield University, Cranfield, Bedfordshire MK43 0AL, United Kingdom.

[c] Electron Microscopy Suite, Faculty of STEM, Open University, Milton Keynes MK7 6AA, United Kingdom.

*Corresponding Email: manzar.sohail@sns.nust.edu.pk

Abstract

The design of a cost-effective, stable, and efficient electrocatalyst for electrochemical water splitting is crucial for hydrogen generation. Non- and compositionally flexible Perovskites are a promising class of catalysts for catalyzing electrochemical water splitting. Herein, we report the synthesis of $La_{0.95}Pr_{1.05}CuO_4$ raw (LPC-R) by the sol-gel method. Then, its surface reconstruction was done by immersing the catalyst in different concentrations of reductive sodium borohydride solution. As a result, an amorphous layer formed on the surface of the catalyst, as observed in scanning electron microscopy (SEM) and High-resolution transmission electron microscopy (HRTEM). The best catalyst, $La_{0.95}Pr_{1.05}CuO_4$ (LPC-2), surface reconstructed by using 2 M sodium borohydride solution, was tested as a bifunctional catalyst and exhibited the lowest overpotential of 260 mV, 104 mV, and Tafel slopes of 54 mVdec−1 and 122 $mVdec^{-1}$ for oxygen evolution reaction (OER) and hydrogen evolution reaction (HER), respectively. Moreover, it also exhibited more than 10 hours of stability. Surface reconstruction tailored electronic structure, and ion stoichiometry form active surface species that contribute to enhancing the catalyst's activity. This work illustrates an efficient strategy of surface reconstruction to improve the performance of as-synthesized catalysts for electrochemical water splitting.

Keywords:

Perovskite Oxides; Surface Treatment with Sodium Borohydride; Surface Reconstruction; Oxygen Vacancies; Bifunctional Catalyst.

Published by Springer. This is the Author Accepted Manuscript issued with: Creative Commons Attribution License (CC:BY 4.0).
The final published version (version of record) is available online at DOI:10.1039/d5nr03432a. Please refer to any applicable publisher terms of use.

1. INTRODUCTION

Fossil fuel depletion, energy shortages, and global warming are significant challenges facing the modern world. These issues can threaten human survival, making it crucial to develop non-carbon renewable energy technologies [1]. Hydrogen is a renewable and clean energy carrier that exhibits a higher energy density, making it a well-suited fuel to meet future energy demands [2]. Electrocatalytic water splitting is a novel approach to hydrogen fuel production [3]. In a water-splitting electrolyzer, the oxygen evolution reaction (OER) and hydrogen evolution reaction (HER) occur at anodic and cathodic electrodes, respectively. However, the sluggish kinetics of both OER and HER result in higher overpotentials and energy losses. RuO_2/IrO_2 and Pt/C are the state-of-the-art catalysts for OER and HER, respectively; however, their poor stability, scarcity, and higher cost limit their applications [4].

Perovskite Oxides are the emerging materials, with the general formula ABO_3; here, the A site is occupied by alkaline earth metal or rare earth metal elements, whereas transition metal elements occupy the B site. Higher stability, structural and compositional tunability, and the capability to control dopant amount at the target site make them among the best materials for the water splitting reaction [5, 6]. Researchers have made significant efforts to improve the efficiency of Perovskite oxides, among which surface reconstruction has proven its efficacy in enhancing electrochemical activity by tailoring the electronic structure and inducing vacancies. As OER and HER depend on the physicochemical properties of the electrolyte interface/electrode surface, a simple and efficient method of surface treatment can improve the efficiency of the catalyst. Recently, several methods for surface treatment of Perovskites have been reported.

For example, Zong et al. reported the surface reconstruction of $La_{0.6}Sr_{0.4}Co_{0.2}Fe_{0.8}O_{3-\delta}$ via selective acid etching. The acid-etched electrocatalyst exhibits higher OER activity due to the formation of oxygen vacancies [7]. Chen et al. utilized magnetron sputtering to fabricate an amorphous layer of $Ba_{0.5}Sr_{0.5}Co_{0.8}Fe_{0.2}O_{3-}$ (BSCF) on a Ni foam substrate. This surface-reconstructed catalyst exhibits enhanced OER activity as compared to crystalline BSCF [8]. Similarly, Lam et al. synthesized $La_{0.8}Sr_{0.2}CoO_{3-\delta}$ (LSC) by the sol-gel method and then treated it with H_2O_2 for surface reconstruction. H_2O_2 treatment forms an amorphous layer, which lowers the overpotential and Tafel slope of LSC [9]. Zhang et al. induce surface reconstruction in $LaNi_{0.75}Fe_{0.25}O_3$ by incorporating F anion by fluorination annealing. Anion incorporation induces

surface reconstruction to produce an oxyhydroxide layer on the surface of the perovskite oxide, which lowers the energy barrier and hence enhances OER activity [10]. Hence, various strategies such as doping [11], plasma treatment [12], amorphization [8], and high-temperature reduction [13] have been employed for the surface treatment to enhance the activity of perovskite oxides.

Here, we present an approach to engineer the surface of perovskite oxide $La_{0.95}Pr_{1.05}CuO_4$ by the sodium borohydride reduction method and investigate the effect of surface reconstruction on the morphology, structure, and catalytic properties of as-synthesized perovskite oxide. Praseodymium (Pr) is substituted at the A site because it is corrosion-resistant in basic solutions, which improves its stability and long-term activity. Additionally, Pr substitution reduces the bond length of Cu-O due to its smaller radius compared to La^{3+} [14]. Furthermore, the partially filled 4f orbitals of Pr^{3+}, hybridize with O 2p and Cu 3d valence electrons and induce variations in electronic states at the Fermi level, which affect OER activity. To our knowledge, $La_{0.95}Pr_{1.05}CuO_4$ has not been reported for water electrolysis to date.

After synthesizing the perovskite oxide, i.e., $La_{0.95}Pr_{1.05}CuO_4$ (LPC-R), its surface reconstruction was done to enhance its catalytic activity for water electrolysis by immersing the as-synthesized catalyst in $NaBH_4$ solution. With the help of SEM and HRTEM, we demonstrate that after $NaBH_4$ reduction, an amorphous layer was formed on the surface of the catalyst. Compared to LPC-R, the reduced catalyst LPC-2 exhibits higher activity (overpotential of 260 mV and 104 mV for OER and HER, respectively). The enhanced activity originated from the reduction of Cu^{+2} to Cu^{+1}, generating oxygen vacancies, a faster electron transport rate, an optimized electronic structure, and the formation of active sites.

2. EXPERIMENTAL SECTION

2.1 Materials

Praesmodymium nitrate hexahydrate $Pr(NO_3)_3 \cdot 6H_2O$, lanthanum nitrate hexahydrate $La(NO_3)_3 \cdot 6H_2O$, cupper nitrate hexahydrate $Cu(NO_3)_2 \cdot 6H_2O$, ethylenediaminetetraacetic acid (EDTA), citric acid ($C_6H_8O_7$), ethanol (C_2H_5OH), sodium borohydride ($NaBH_4$), nafion and deionized water (DI) were purchased from Sigma Aldrich and used without further purification.

2.2 Synthesis of $La_{0.95}Pr_{1.05}CuO_4$

$La_{0.95}Pr_{1.05}CuO_4$ was synthesized by a sol-gel method. $Pr(NO_3)_3 \cdot 6H_2O$, $La(NO_3)_3 \cdot 6H_2O$, and $Co(NO_3)_2 \cdot 6H_2O$ were dissolved in DI water, followed by the addition of citric acid and EDTA. The molar ratio of the total metal ions, citric acid, and EDTA was maintained at 1:2:1. The solution was constantly stirred at 80 °C for about 3 h until the formation of a viscous gel. The gel was dried at 200 °C for 3 h and then calcined at 600 °C under air for 5 h at a heating rate of 5 °C min^{-1}. The sol-gel method is widely used to synthesize high-purity, homogenous nanostructures, and the specialty of this method is reproducibility. The as-synthesized catalysts $La_{0.95}Pr_{1.05}CuO_4$ raw powder were named as LPC-R.

2.3 Surface Reconstruction of LPC-R

For surface reconstruction of LPC-R, different concentrations of $NaBH_4$ solution (1 M, 1.5 M, and 2 M) were prepared. Then, 0.3g of as-synthesized LPC-R was added to 30 mL of each of the $NaBH_4$ solution concentrations. These solutions were stirred for 1 h at 60 °C, then washed with ethanol and DI water. Surface-reconstructed samples were designated as LPC-1, LPC-1.5, and LPC-2, corresponding to $NaBH_4$ concentrations of 1, 1.5, and 2 M, respectively. As a result of surface reconstruction, oxygen vacancies were created as shown in **Figure 1**.

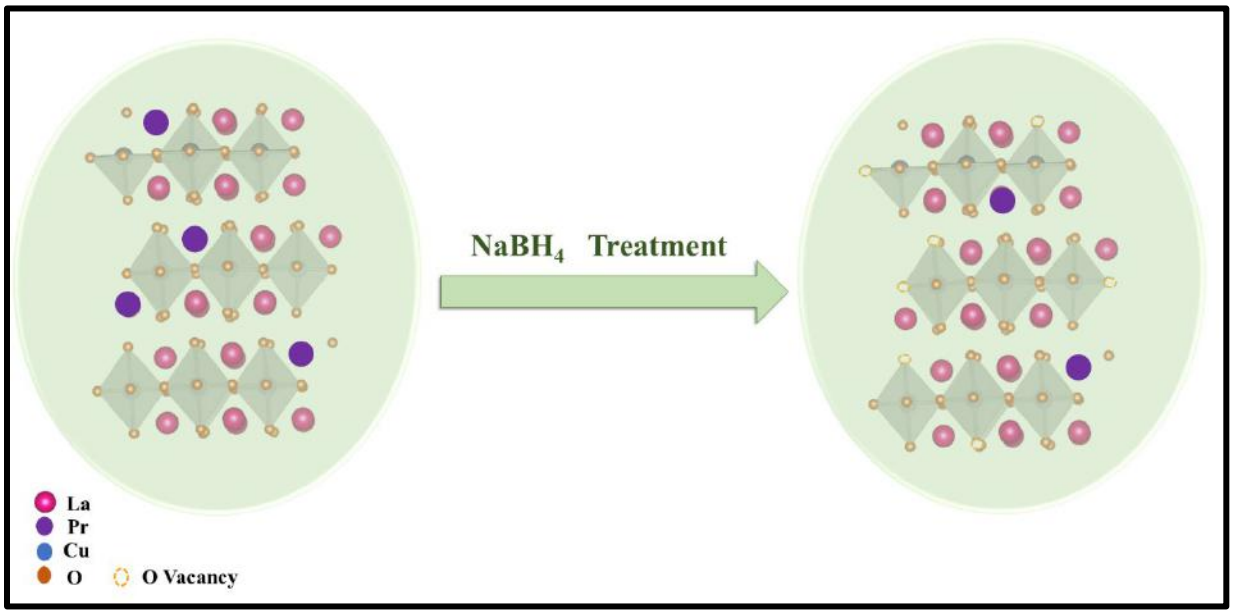


Figure 1: Surface Reconstruction of $La_{0.95}Pr_{1.05}CuO_4$

2.4 Characterization of LPC Perovskite Oxides

The crystallinity and composition of as-synthesized samples were analysed using powder X-ray diffraction (p-XRD) on Bruker D8 Advance diffractometer. Measurements were performed using Cu Kα (γ = 1.54 Å) over a 2θ range of 10°–90° with a 0.05° step size. The operating current and working voltage were set to 40 mA and 40 kV, respectively. The sample morphology was examined by scanning electron microscopy (SEM) on a Tescan S8000 FEG SEM. Images were captured with a beam current of 100 pA and an accelerating voltage of 20 kV. For SEM sample preparation, the as-synthesized powders were sonicated in ethanol and then deposited onto a carbon tape substrate. After drying, a 10 nm gold coating was applied to enhance conductivity. High-resolution transmission electron microscopy (HRTEM) was used to investigate the sample morphology and lattice fringes further. HRTEM was done on a JEOL 2100 HRTEM operating at 200 kV with an 11 Mpx Gatan Orius in-line digital camera. The valence states and chemical composition were investigated using X-ray photoelectron spectroscopy (XPS) with a Thermo K-Alpha. Al K_{alpha} (1487 eV) is used as a monochromatic source with an overall energy resolution of 350 MeV. The instrument's onboard charge compensation system was used for all samples. Survey scans were carried out in each corner of the sample to check for homogeneity, with a dwell time of 250 ms and a step size of 0.5 eV. Subsequently, high-resolution scans were performed for the elements of interest, using a 250 ms dwell time, a 0.1 eV step size, and a 20 eV pass energy. This examination provides insights into the sample's chemical states and surface composition. Nitrogen (N_2) adsorption–desorption was used to examine the surface area after surface reconstruction using the 3P Meso 222 instrument. The Brunauer-Emmet-Teller (BET) method was employed to find the surface area, whereas pore size distribution curves were calculated by the Barret-Joyner-Halenda (BJH) method.

2.5 Electrochemical Measurements

The electrochemical measurements were performed in a three-electrode setup using an electrochemical workstation IVIUMSTAT Electrochemical Interface. 1.0 M KOH (pH = 14) was used as an electrolyte, and all measurements were performed at room temperature. Saturated Ag/AgCl (1 M KCl) as reference, Pt wire as counter, and Ni foam was used as a working electrode. Ni foam was washed by sonicating it in 3.0 M HCl, ethanol, and water for 15 min., respectively. To prepare the catalyst ink, 5 mg of perovskite powder was dispersed in 2 mL of ethanol, 10 µL of

Nafion was added as a binder, and the mixture was sonicated for 30 min. Then, Ni foam was coated with this ink using the drop-casting method and dried in an oven at 50 °C overnight.

Linear sweep voltammetry (LSV) was performed against a silver electrode (Ag/AgCl) at a scan rate of 10 mV/s. The following equation I was used for the conversion of Ag/AgCl to RHE.

$$\mathbf{E_{RHE} = E_{Ag/AgCl} + E^{o}_{Ag/AgCl} + 0.059pH} \qquad \mathbf{(I)}$$

The Tafel slope was calculated by fitting the linear regions of the LSV curve in the Tafel equation II [15].

$$\mathbf{\eta = b \log J + a} \qquad \mathbf{(II)}$$

Here, b is the Tafel slope. The active surface area of the as-synthesized catalyst was calculated using cyclic voltammetry (CV) scans performed in the non-faradaic region at different scan rates: 5, 10, 25, 50, 75, and 100 mV/s. The scan rate was plotted against the ΔJ (which is half of the capacitive current ($J_{anodic} - J_{cathodic}/2$)), the slope of this graph gives double layer capacitance (C_{dl}). The electrochemically active surface area (ECSA) was determined by using the following equation III.

$$\mathbf{ECSA = A \times C_{dl} / C_s} \qquad \mathbf{(III)}$$

Here,

A (cm^2) = area of working electrode, i.e., 1 cm^2, C_{dl} is double layer capacitance in $mF.cm^{-2}$, and C_s is specific capacitance, which is 0.04 $mF.cm^{-2}$. The electrochemical impedance spectroscopy (EIS) was performed in the frequency range of 100 kHz to 100 mHz. A catalyst stability test was conducted using Chronopotentiometry (CP) at a constant current of 10 $mAcm^{-2}$.

3. RESULTS AND DISCUSSION

The p-XRD diffractograms of as-synthesized $La_{0.95}Pr_{1.05}CuO_4$ (LPC-R, LPC-1, LPC-1.5, and LPC-2) are shown in **Figure 2(a)**. The tetragonal perovskite structure of LPC is well-matched with JCPDS 54-0856, and it exhibits space group I4 *mmm (139).* It is shown that a pure phase is formed, and there is no difference between the diffraction patterns of LPC-R and treated catalysts (LPC-1, LPC-1.5, and LPC-2). The characteristic peaks of (101), (104), (103), (110), (114), (105), (006), and (200) appear at 23.4◦, 28.9◦, 31.2◦, 31.7◦, 43.0◦, 43.4◦, 43.9◦, and 44◦, respectively, which is

consistent with the standard pattern of $La_{0.95}Pr_{1.05}CuO_4$. The d-spacings calculated from the (103) and (110) diffraction peaks are 0.286 nm and 0.281 nm, respectively; detailed lattice parameters are explained in **Table S3**. The crystallite size was calculated using the Scherrer formula for LPC-R, which yielded a value of 1.10 nm. As shown in Figure 2(a), surface treatment with sodium borohydride reduces the peak intensity and increases peak broadening, leading to a decrease in crystallite size. As shown in the enlarged p-XRD pattern **Figure 2(b)**, from 28◦ to 34◦, the diffraction peaks are shifted to a lower angle, which indicates the expansion of the crystal lattice after surface treatment. This expansion could generate oxygen vacancies [7]. A new peak has appeared at 30.2◦, which is due to the (200) lattice plane of sodium borohydride [16]. It can be assumed that the LPC perovskite is successfully synthesized, and its crystal structure remains well-preserved after surface treatment.

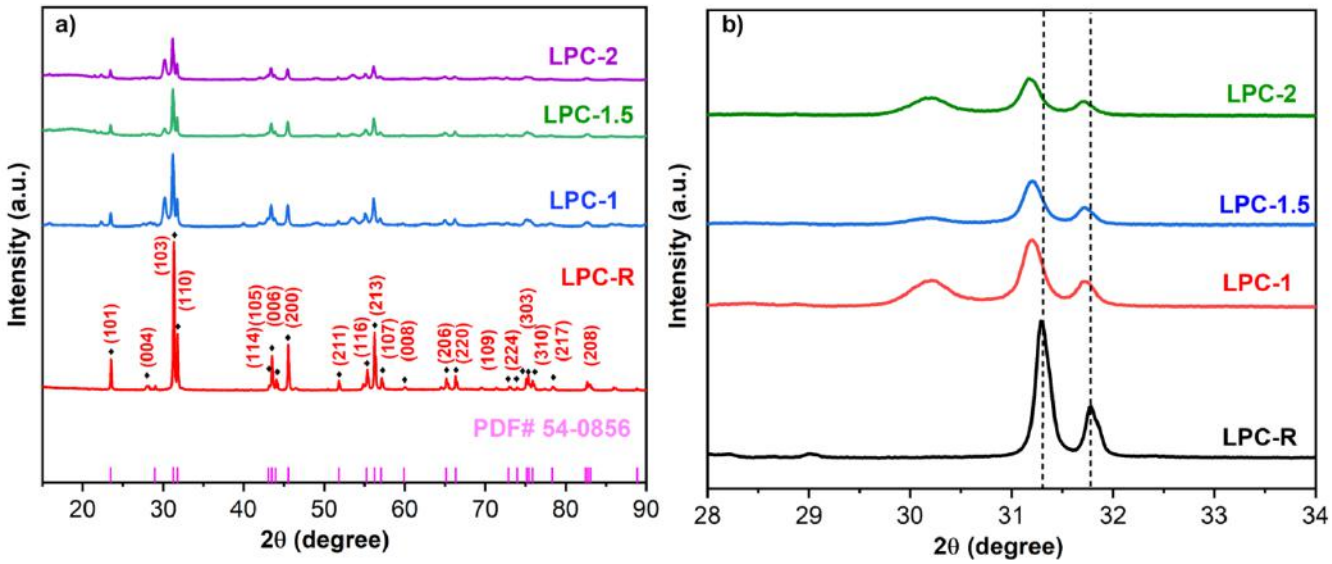


Figure 2: (a) p-XRD Diffractograms of LPC-R, LPC-1, LPC-1.5, and LPC-2, which show a close comparison to $La_{0.95}Pr_{1.05}CuO_4$ (JCPDS 54-0856). (b) Magnified representative 2θ region showing the peak shifts in (103) and (110).

SEM was used for the morphological analysis of the samples. As seen in **Figure 3(a),** the untreated catalyst (LPC-R) exhibits open reticular morphology. After the $NaBH_4$ reduction treatment, the as-synthesized catalysts retained their morphology but underwent surface reconstruction, resulting in a rougher surface that created more pores. It can be seen in **Figure 3** that the surface of the treated

catalysts becomes exfoliated, and LPC-2 exhibits a more porous nature than LPC-1 and LPC-1.5. **Figure S1** shows the SEM images of the as-synthesized samples at higher resolution, which also reveal the porosity of the catalyst. For confirmation of elemental composition and distribution, EDX and elemental mapping were performed. Figures S2, S3, S4, and S5 demonstrate that the as-synthesized samples contain all four elements, namely La, Pr, Cu, and O, while the presence of Au is attributed to the gold coating for SEM analysis. Elemental mapping shows homogeneity and even distribution of elements.

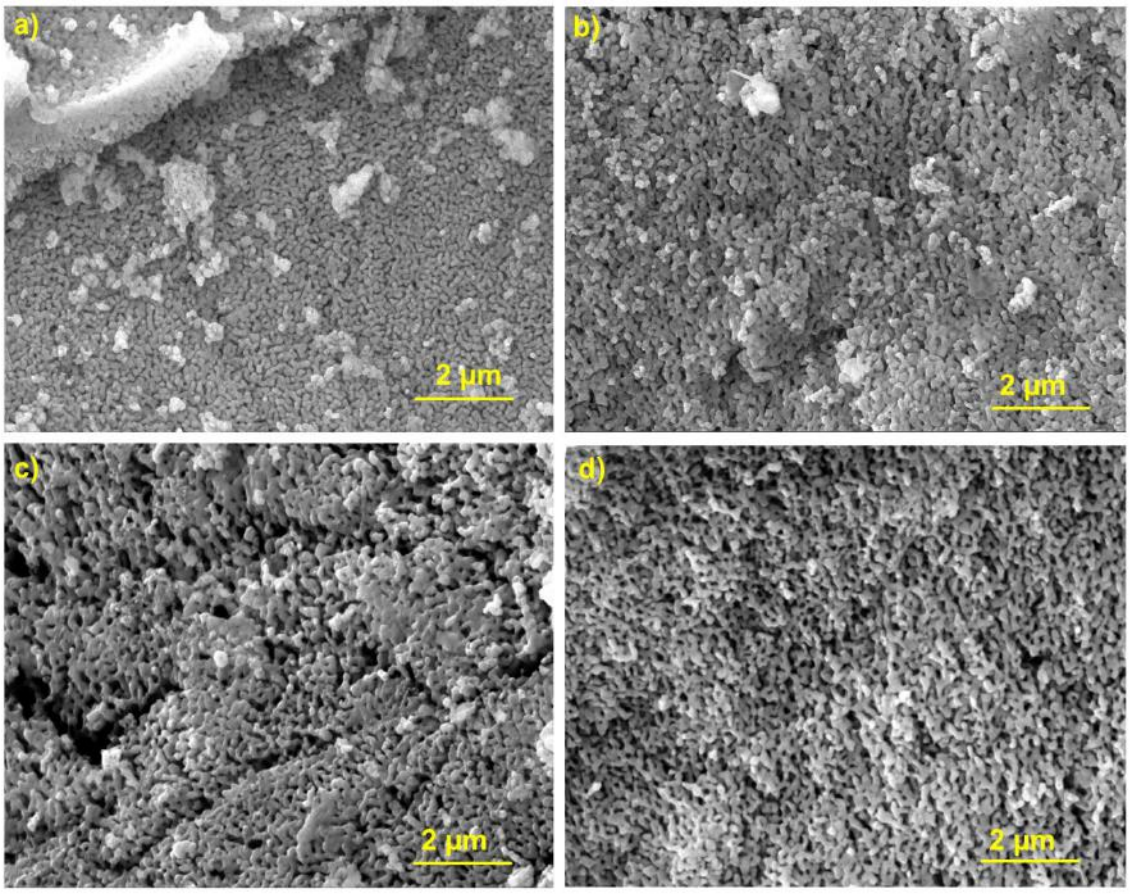


Figure 3: SEM images of (a) LPC-R (b) LPC-1 (c) LPC-1.5 (d) LPC-2

The morphologies of LPC-R and LPC-2 were further characterized by HRTEM. As shown in **Figure 4(a),** LPC-R has a uniform, smooth surface with well-defined lattice fringes. In contrast, after surface reconstruction, an amorphous layer is formed, which is evident from the lack of discernible lattice fringes, as shown in **Figure 4(b),** although perovskite retains its structure. These results confirm that surface reconstruction occurs after sodium borohydride treatment.

The selected area electron diffraction (SAED) patterns in **Figure 4(c)** show that LPC-R exhibits distinct diffraction rings, confirming its crystalline structure, whereas LPC-2 exhibits a blurred halo, which is due to an amorphous layer formed on the surface, as shown in **Figure 4(d).** The bright spots in the SAED pattern of LPC-R correspond to lattice planes (105), (200), and (213), which exhibit the d-spacings of 0.20 nm, 0.19 nm, and 0.16 nm, respectively. These values match those calculated from p-XRD for the d-spacing. On the other hand, SAED of LPC-2 also shows concentric circles, but bright spots are noticeably weaker; these spots correspond to (208), (213), and (110) lattice planes, exhibiting d-spacings of 0.12 nm, 0.16 nm, and 0.28 nm, respectively. These weaker spots reveal that LPC-2 exhibits a disordered lattice, indicating a surface reconstruction on the surface of LPC-2. p-XRD and SAED further confirm that the crystalline phase of the catalyst remains unchanged and $NaBH_4$ treatment only influences the surface of LPC-2 [17].

HRTEM images of LPC-R, shown in **Figure 5(a),** demonstrate clear lattice fringes. The inset displays an inverse fast Fourier transform (FFT) image, used to measure the distance between the fringes, which reveals an interplanar distance of 0.281 nm corresponding to the (110) plane of LPC-R. **Figure 5(b)** shows the HRTEM image of LPC-2, which confirms the presence of an amorphous layer as indicated by the blurred lattice fringes. The inverse FFT image also confirms this in the inset, which demonstrates the blurred nature of the lattice fringes. The distance between these fringes indicates an interplanar distance of 0.37 nm, as shown in the profile graphs of the inverse FFT (Figures 5(c) and 5 (d)), corresponding to the (101) lattice plane of the p-XRDs of LPC-R and LPC-2. These observations support the p-XRD results, confirming the crystallization and surface reconstruction in LPC-R and LPC-2, respectively.

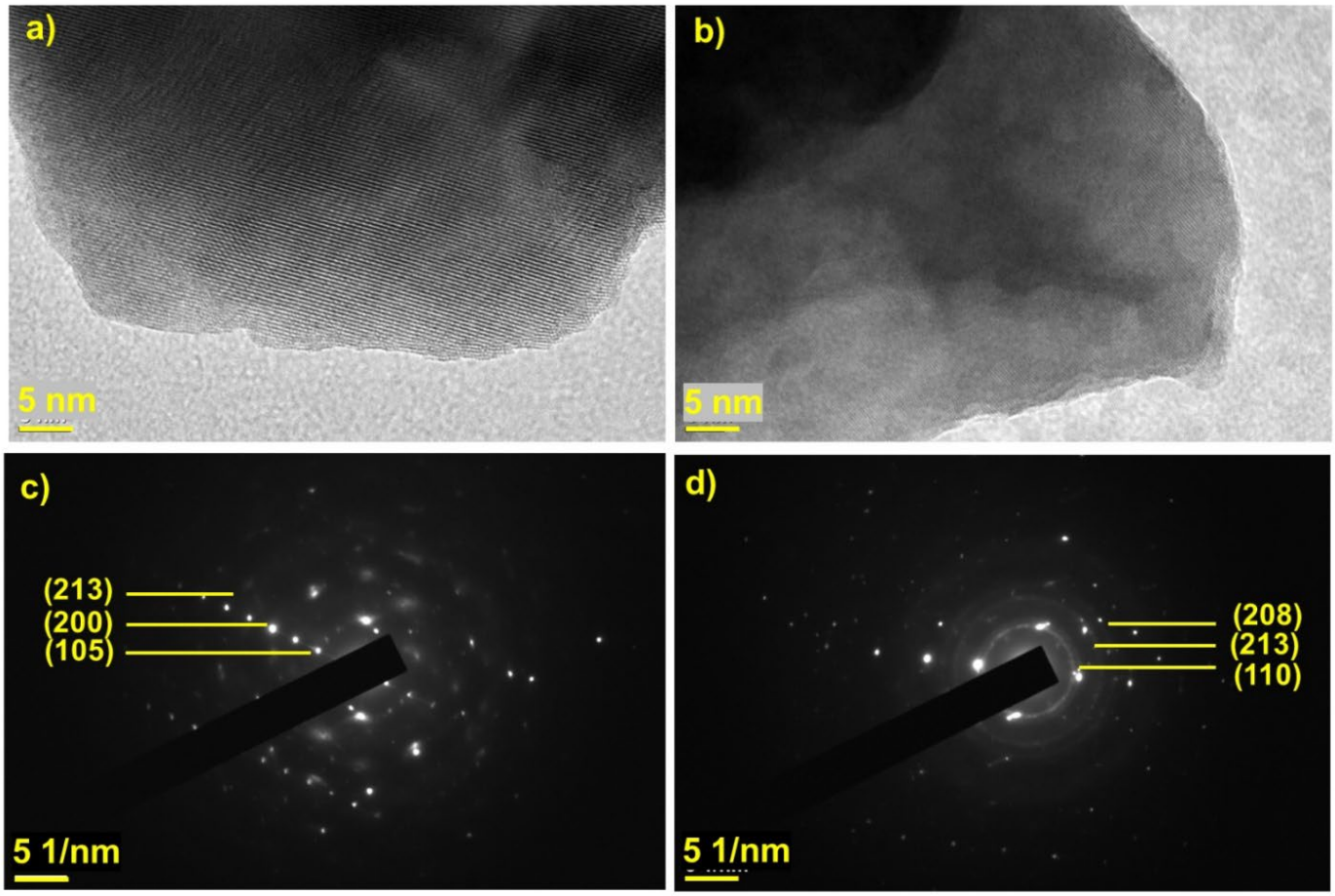


Figure 4: HRTEM images of (a) LPC-R and (b) LPC-2 with corresponding SAED patterns of (c) LPC-R and (d) LPC-2

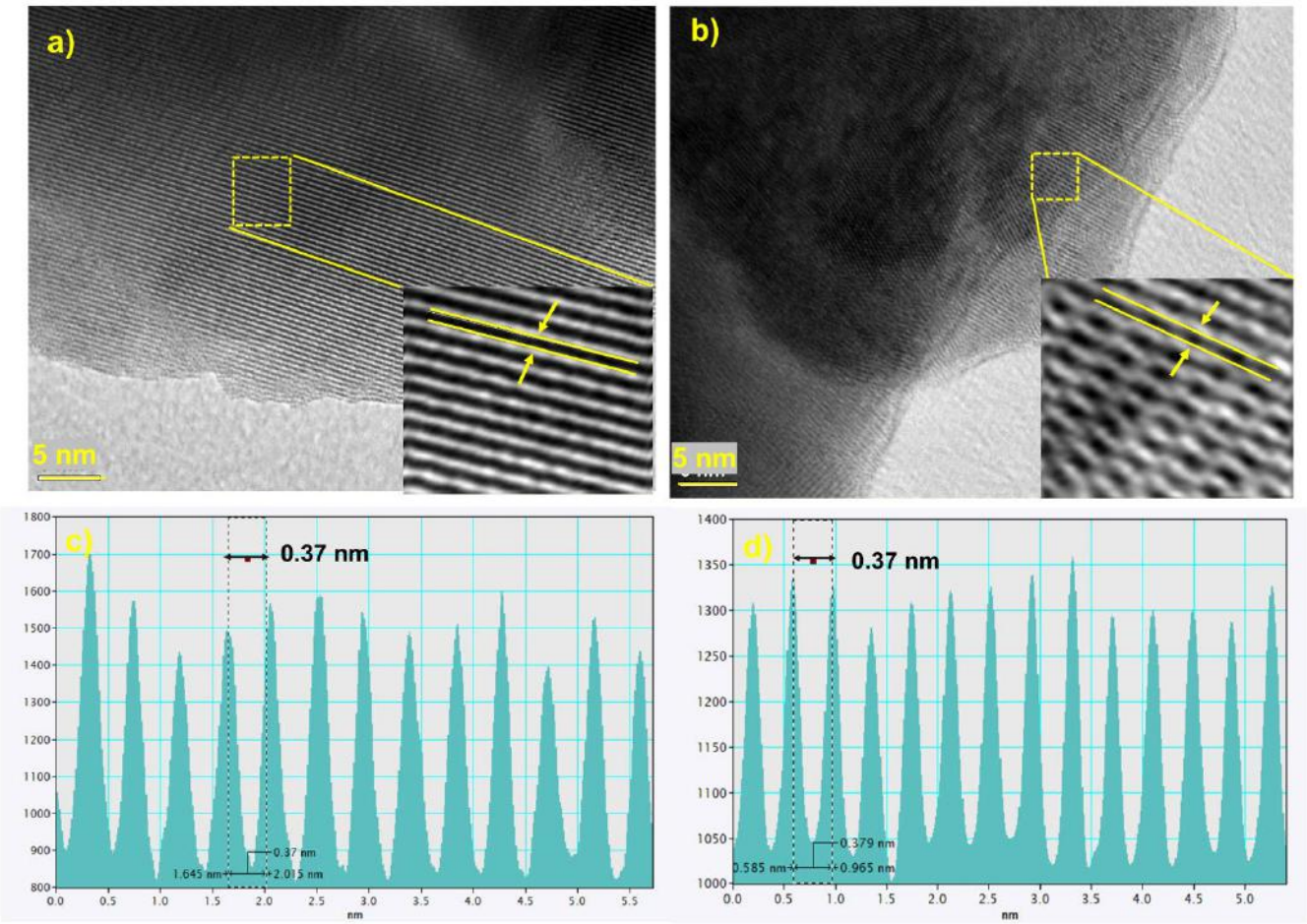


Figure 5: (a) HRTEM image of LPC-R with the inset showing the corresponding inverse FFT. (b) HRTEM image of LPC-2 with an inset showing the corresponding inverse FFT. (c-d) Profile graphs of the insets in (a) and (b).

Surface area and porosity are two key factors that significantly impact a catalyst's efficiency. To investigate both these factors, N_2 adsorption-desorption isotherms were performed. LPC-2 exhibits a Type IV isotherm, as shown in Figure 6(a). The BET specific area was measured to be 15.15 m^2/g, compared to LPC-R, which has a lower BET surface area of 3.97 m^2/g, as shown in Figure S6**(a)**. Furthermore, Barrett-Joyner-Halenda (BJH) pore size distribution in **Figure 6(b)** demonstrates that LPC-2 exhibits a pore diameter of 3.8 nm, which is less than the pore diameter of LPC-R, as displayed in **Figure S6 (b)**. These results demonstrate that LPC-2 exhibits more surface area, which leads to more reaction sites and enhanced efficiency.

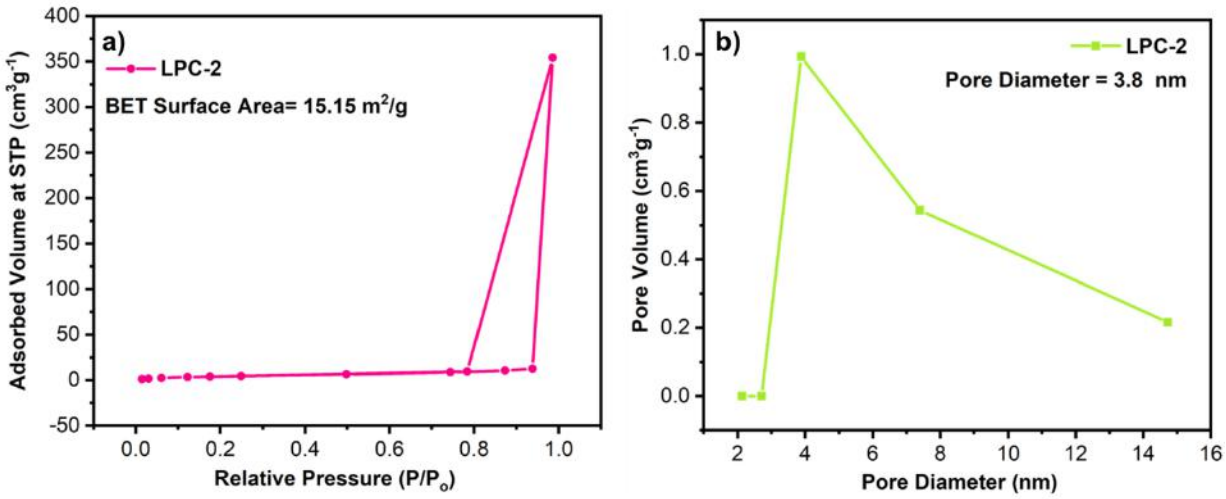


Figure 6: (a) N_2 adsorption-desorption isotherms of LPC-2. (b) Pore size distribution curves of LPC-2.

Since HER and OER are the electrolyte-catalyst interface reaction, the surface chemical state of the as-synthesized catalyst is of paramount importance [18]. XPS was used to study the electronic states of atoms present on the surface. A survey scan of LPC-R and LPC-2 confirmed the presence of La, Pr, Cu, and O. **Figure 7(a)** shows a survey scan of LPC-R and LPC-2. **Figure 7(c)** shows the high-resolution spectra of Pr and Cu, as the Pr 3d and Cu 2p signals overlap, so both are combined into a single spectrum. The asymmetric and broad Pr $3d_{5/2}$ and Cu $2p_{3/2}$ signals were deconvoluted into three peaks positioned at 928.8, 932.0, and 934.1 eV. These peaks are assigned to Pr^{3+}, Cu^0/Cu^+ ,and Pr^{4+} [19]. Peak at 943 eV in LPC-R indicates the presence of $Cu^{2+,}$ while this peak is absent in LPC-2, showing the complete reduction of $Cu^{2+.}$ Due to the overlapping of Cu 2p and Pr 3d spectra, the XPS spectra of Pr $3d_{5/2}$ and Cu $2p_{3/2}$ were deconvoluted with constraints of peak parameters of Pr and Cu signals to obtain accurate peak positions.

To identify the chemical state of Cu, Cu Auger LMM XPS spectra were also obtained. The Auger LMM of Cu in **Figure 7(e)** indicates peak position 568.6 eV for LPC-R and 570.5 eV for LPC-2, which confirms the presence of Cu^{2+} in LPC-R and Cu^{1+} in LPC-2 [20]. Since the obvious peak shift of 1.9 eV is being observed.

High resolution XPS spectra of La 3d, as shown in **Figure 7(b),** exhibits doublet satellite structure for La^{3+} LPC-R exhibits three peaks for La $3d_{5/2}$ centered at 831.9 eV, 834.3 eV and 837.1 eV while LPC-2 exhibits two peaks with a positive chemical shift of 0.5 eV due to higher oxygen vacancies

on its surface, these oxygen vacancies increases effective nuclear charge which leads to positive chemical shift in XPS spectra [21, 22]. A peak at 831.9 eV in LPC-R, while no peak at this position is observed in LPC-2, this peak corresponds to the bulk oxide state in LPC-R, which is being converted to the surface oxide state in LPC-2 [23]. Electrons transfer from O 2p valence band to La 4f unoccupied orbital leads to La 3d shake-up state, which results in splitting of peaks [24].

O 1s spectra of LCF-R and LCF-2 show three peaks centered at (532.8 vs 532.0 eV, 530.9 vs 531.2 eV, 528.0 vs 528.4 eV). The binding energies at 532.0, 531.0, and 528.0 eV can be attributed to H_2O, O_2^{2-}/O^- or -OH (O_{ads}) and O^{2-} (O_{latt}) [18, 25]. O_2^{2-}/O^- are the active oxygen species which relate to oxygen vacancies and hence play an essential role in enhancing OER [26, 27], as the rate-determining step in the OER reaction produces O-O from OOH [28, 29], and more -OH on the surface of the catalyst facilitates the OER reaction [30, 31]. As can be seen in **Figure 7(d),** the peak intensity of LPC-2 is higher than that of LPC-R, which confirms the presence of more oxygen vacancies in LPC-2 and hence enhances the reaction.

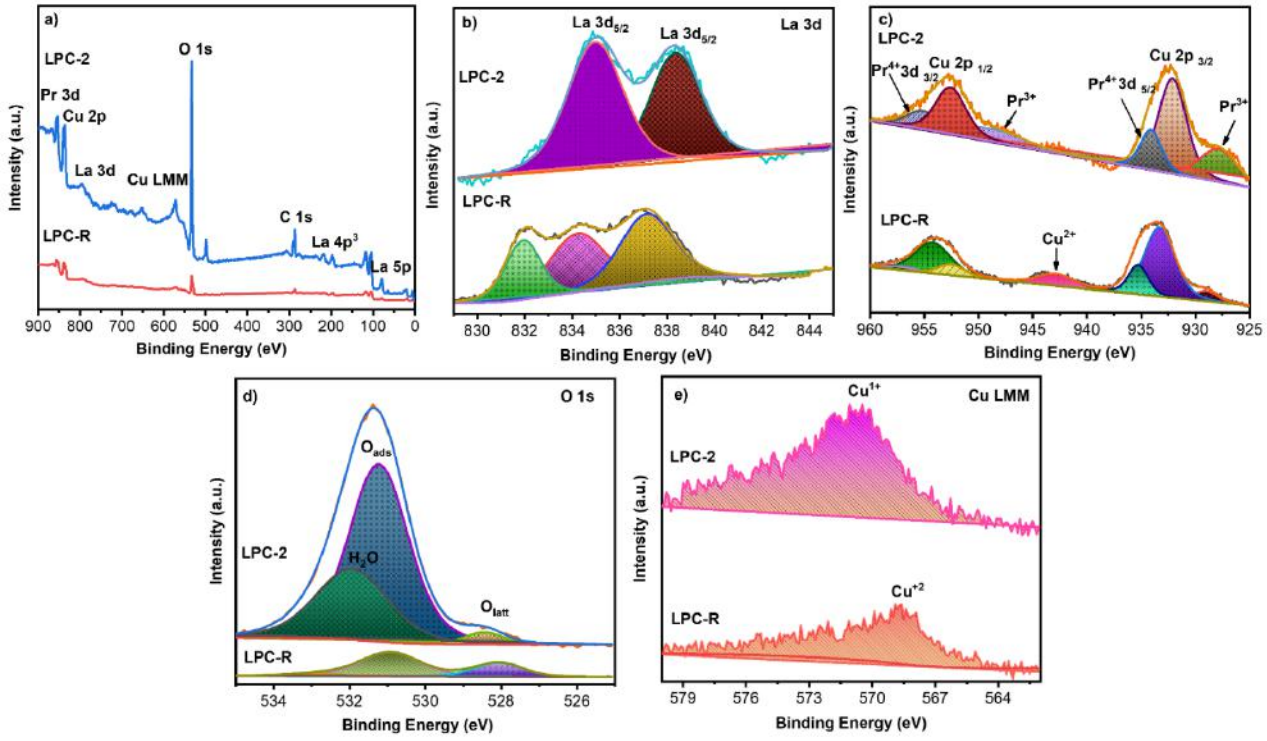


Figure 7: XPS analysis of LPC-R and LPC-2: (a) survey scan, (b) high-resolution spectra of La 3d (c) high-resolution spectra of Cu 2p and Pr 3d, (d) O 1s spectra, (e) Cu LMM Auger peaks.

3.1 Electrochemical Activity

The electrochemical activity of the as-synthesized catalyst was tested in 1 M KOH solution. OER activities of raw (LPC-R) and treated catalysts were investigated by LSV. Polarization curves in **Figure 8(a)** show that LPC-2 exhibited enhanced electrocatalytic activity as compared to LPC-1.5, LPC-1, and LPC-R. Overpotential (η_{10}) is also an important parameter to investigate the activity of a catalyst. It is the potential that is required to produce 10 $mAcm^{-2}$ current density, which is equivalent to 10% of solar energy conversion efficiency [32]. The reverse polarization curve of LPC-2 in Figure 8(b) shows that LPC-2 exhibits an overpotential of 260 mV, which is lower than the overpotentials of LPC-R, LPC-1, and LPC-1.5, i.e., 455, 446, and 432 mV. The bar graph of overpotential at 10 and 100 $mAcm^{-2}$ is shown in **Figure 8(c)**. It is observed that LPC-2 exhibits a smaller η10 value than its counterparts, indicating that LPC-2 is a more effective OER catalyst. The Tafel slope estimates reaction kinetics; a smaller value of the Tafel slope indicates faster reaction kinetics and ultimately higher electrocatalytic activity. The Tafel slope was calculated from the potential linear dependence versus log(j). It can be seen in **Figure 8(d)** Tafel slopes of LPC-R, LPC-1, LPC-1.5 and LPC-2 are 231 $mVdec^{-1}$, 179 $mVdec^{-1}$, 103 $mVdec^{-1}$ and 54 $mVdec^{-1}$ respectively. Surface reconstruction by sodium borohydride treatment produces oxygen vacancies, which significantly improve the performance of LPC-2.

ECSA and electrochemical double-layer capacitance (C_{dl}) can be measured from CV curves. **Figure S7 (a)** shows that LPC-2 exhibits the highest value of $C_{dl,}$ i.e., 0.586 $mFcm^{-2}$, compared to LPC-R, LPC-1, and LPC-2. ECSA calculated from C_{dl} is 4.2 cm^2, 10.4 cm^2, 11.6 cm^2 and 15.1 cm^2 for LPC-R, LPC-1, LPC-1.5 and LPC-2 respectively as shown in bar graph **Figure S7 (b)**. Reaction kinetics can be investigated by EIS. It measures the charge transfer resistance (R_{ct}) and relates it to the electrocatalytic activity of the catalyst [33]. CPE with a diffusion circuit is used to fit the EIS of as-synthesized catalysts. Here, R_{ct} shows the charge transfer resistance, and R_s represents the electrolyte resistance. It can be seen in **Figure S7 (c)** that the LPC-2 exhibits a lower value of interfacial Rct, i.e., 21 Ω, while the Rct of LPC-R, LPC-1, and LPC-1.5 is 95, 73, and 35 Ω, respectively, demonstrating that LPC-2 exhibits a fast charge transfer rate and good conductivity. Another important parameter to evaluate the performance of an as-synthesized catalyst is to investigate its stability. Therefore, a chronopotentiometric (CP) test was carried out with the best catalyst, i.e., LPC-2, at 10 $mAcm^{-2}$ for 10 h. As displayed in **Figure S7 (d),** the potential of LPC-

2 remains almost constant, which demonstrates that the properties and structure of the catalyst are quite stable during CP analysis. Therefore, it can be concluded that LPC-2 has the potential to become a promising catalyst for practical water splitting.

The efficiency of LPC-2 can be attributed to its reduced Cu^{+1} ions, rough morphology, and higher oxygen vacancies. By $NaBH_4$ reducing treatment, oxygen was removed, and oxygenated compounds were formed, creating delocalized electrons and oxygen vacancies. The excess electrons contributed to the transformation of Cu^{2+} to Cu^{1+}. Reduced Cu enhances the electrical conductivity and directly participates in the desorption and adsorption of intermediates [34]. Pr^{4+}/Pr^{3+} redox flexibility helps in oxygen vacancy formation and charge compensation caused by Cu reduction. The reduction treatment also maximizes the exposure of active sites to reactant molecules and thus enhances electrical conductivity and catalytic activity.LPC-2 exhibits the highest ECSA, the lowest charge transfer resistance, and long-term stability.

OER process is the four-step process, its proposed mechanism under alkaline conditions is:-

$$M + OH^- \longrightarrow MOH + e^- \quad \text{(Eq 1)}$$

$$MOH + OH^- \longrightarrow MO + H_2O + e^- \quad \text{(Eq 2)}$$

$$MO + OH^- \longrightarrow MOOH + e^- \quad \text{(Eq 3)}$$

$$MOOH + OH^- \longrightarrow M + O_2 + H_2O + e^- \quad \text{(Eq 4)}$$

In the first step, OH^- ions get adsorbed on the catalyst's active sites (Eq. 1). In the second step, OH^- ion recombined, resulting in the formation of MO (Eq. 2). This MO forms intermediate MOOH (Eq. 3), which finally combines with another OH^- ions and leads to the formation of O_2 gas (Eq. 4). As the oxygen vacancies created by reduction treatment reduces the energy barrier, enhances charge mobility, improves OH^- adsorption, promotes O-O bond formation for OER and the formation of abundant Cu^{+1} active sites readily form CuOOH, which combines with OH^- and produces O_2.

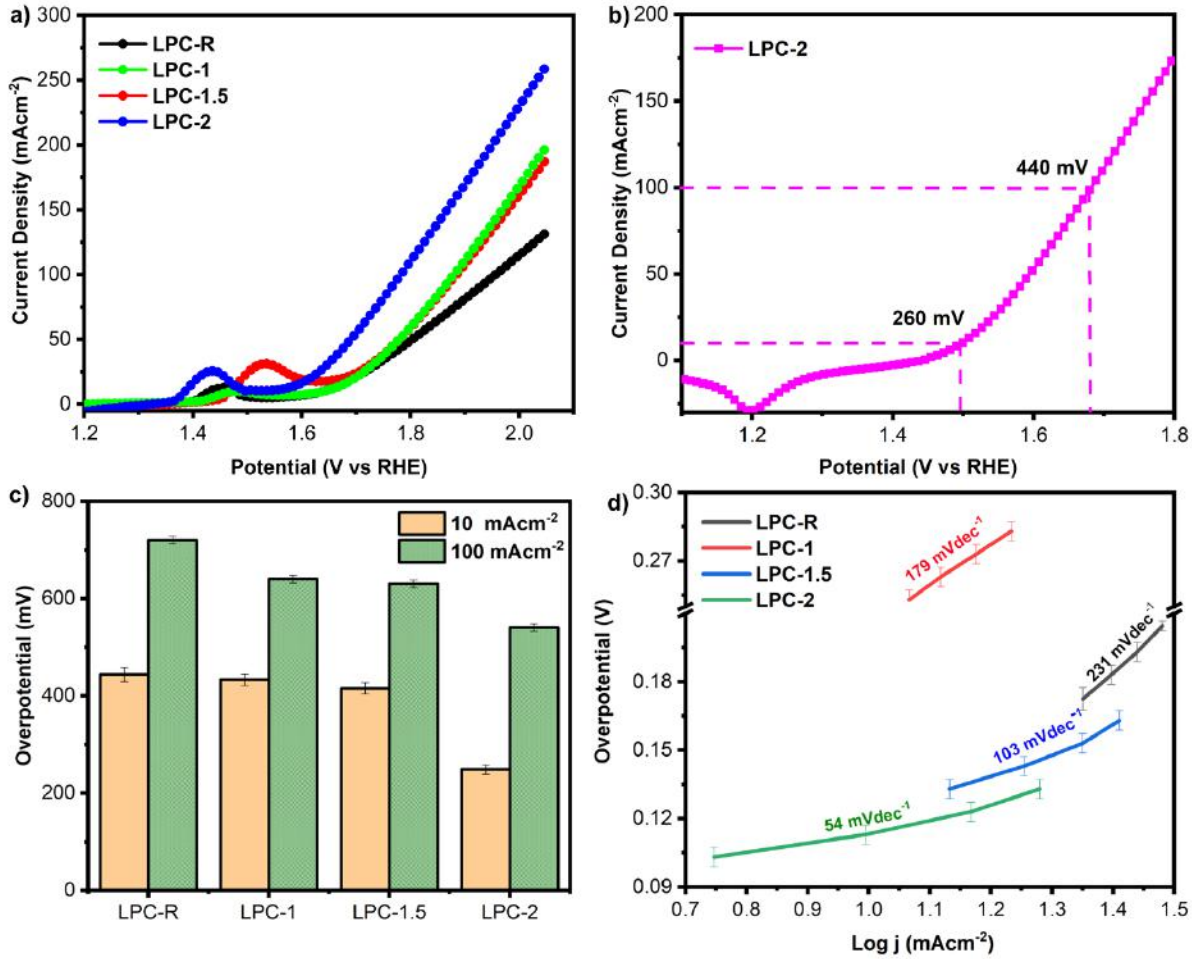


Figure 8: (a) OER polarization curves, (b) Reverse polarization curve of LPC-2, (c) Bar graph of overpotential at 10 and 100 $mAcm^{-2}$, (d) Tafel plot.

To study the HER of the as-synthesized catalyst, the electrochemical measurements are carried out in 1 M KOH solution. **Figure 9(a)** shows the HER polarization curves of as-synthesized samples. It is clearly visible in **Figure 9(a)** that the order of HER activity is the same as OER, i.e., LPC-2 exhibits the lowest overpotential (104 mV@10$mAcm^{-2}$), whereas LPC-R, LPC-1, and LPC-1.5 exhibit overpotentials of 254 mV, 184 mV, and 124 mV@10$mAcm^{-2}$, respectively, as shown in **Figure 9(d)**. The enhanced activity of LPC-2 is confirmed by its smaller value of Tafel slope 122 $mVdec^{-1}$, as compared to other catalysts, i.e., 171 $mVdec^{-1}$, 183 $mVdec^{-1}$, and 213 $mVdec^{-1}$ for LPC-1.5, LPC-1, and LPC-R, respectively, as seen in **Figure 9(c),** demonstrating that LPC-2 exhibits rapid electron transfer. The value of Tafel slope illustrates that HER follows the Volmer-Heyrovsky mechanism:-

Volmer step:

$$H_2O + A + e^- \longrightarrow A\text{-}H_{ads} + OH^- \qquad \text{(Eq 5)}$$

Heyrovsky step:

$$H_2O + e^- + A\text{-}H_{ads} \longrightarrow OH^- + H_2 \qquad \text{(Eq 6)}$$

Here, A represents the active sites on the surface of the electrode, and the H_{ads} are the hydrogen intermediates generated by the discharge of water molecules on the surface of the catalyst (Eq. 5). H_2 gas is evolved through the electrochemical desorption process (Eq. 6) [35].

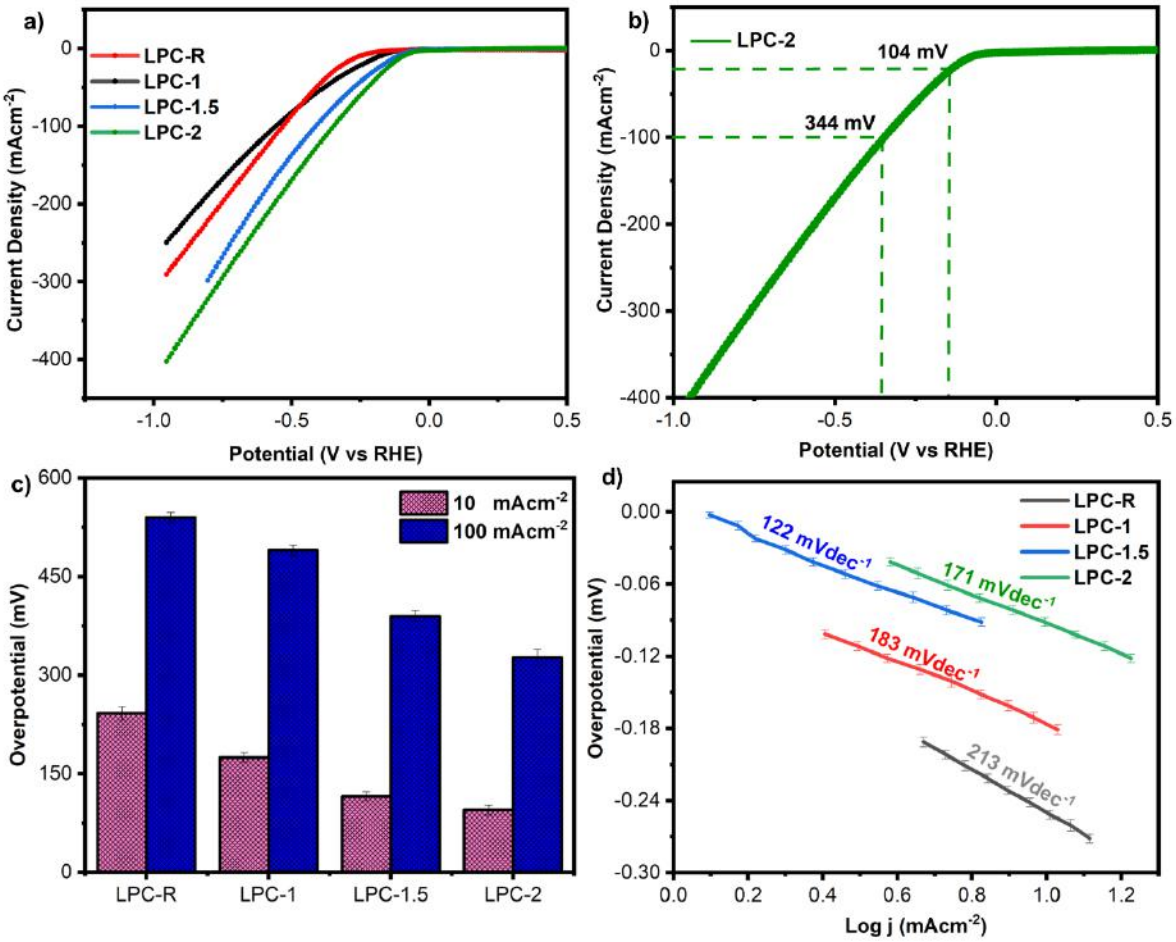


Figure 9: (a) HER polarization curves, (b) Reverse polarization curve of LPC-2, (c) Bar graph of overpotential at 10 and 100 $mAcm^{-2}$, (d) Tafel plot.

Moreover, to explore the factors affecting catalyst activity, ECSA was evaluated from the electrochemical double-layer capacitance (C_{dl}). As seen in **Figure S8 (a)**, LPC-2 exhibits much higher C_{dl} (0.09 $mFcm^{-2}$) as compared to C_{dl} of LPC-R, LPC-1, and LPC-1.5. Similarly, ECSA,

calculated from electrochemical double-layer capacitance and specific capacitance, also shows that LPC-2 exhibits the highest active surface area, as displayed in the bar graph of Figure S8**(b)**. The electron transfer rate was further investigated by EIS. As shown in **Figure S8 (c),** LPC-2 exhibits a lower charge transfer resistance, i.e., 30 Ω, while the Rct of LPC-R, LPC-1, and LPC-1.5 is 150, 110, and 80 Ω, respectively, demonstrating better activity and conductivity in LPC-2.

To evaluate the stability of the best catalyst, i.e., LPC-2, a chronopotentiometric (CP) test was carried out at 10 $mAcm^{-2}$ for 15 hours. As shown in **Figure S8 (d),** LPC-2 exhibits good stability with minimal attenuation. In the CP test, a little bit of an increase in potential is observed, which is attributed to O_2 poisoning; oxygen bubbles produced during CP, destabilize it [36].

These results indicate the superior electrocatalytic activity and faster kinetics of LPC-2, making it a promising bifunctional catalyst for practical applications.

Tables S1 and S2 present a comparison of LPC-2 with the literature, showing that the optimized LPC-2 exhibits the best activity as a bifunctional catalyst among the reported catalysts. Hence, the remarkable activity of LPC-2 towards OER/HER can be attributed to several characteristics. First, the reduction treatment makes its surface rough and porous, which not only provides exposed active sites but also enhances interaction with the electrolyte, aiding the transport of OH^- ions. It also provides a favorable route for electron transport, thereby improving the reaction kinetics, as confirmed by Tafel plots. Second, Cu ions surrounded by oxygen vacancies preferentially adsorb OH--, promoting electron transfer between intermediate reaction species and the catalyst surface, thereby enhancing OER and HER reactions [37].

Jia et al. discovered that high-conductivity oxides could be created by forming interfaces with mixed valences. These interfaces allow the mobility and high concentration of electrons at the interface of the amorphous surface layer and the crystalline layer. At this junction, the amorphous surface layer donates electrons and the crystalline layer serves as a transport channel for electrons [38]. Furthermore, after surface reconstruction, the surface area of the perovskite oxide increases due to the formation of an amorphous layer, which enhances wettability to the electrolyte and hence reduces the electron transport path. In summary, a suitable concentration of oxygen vacancies and a defect-rich surface enhance the electrocatalytic activity of LPC-2 for both OER and HER. A lower concentration of oxygen vacancy would not generate enough active sites for reaction, while too many oxygen vacancies would destroy the electronic structure, resulting in a poor activity [39].

Conclusion

In conclusion, $La_{0.95}Pr_{1.05}CuO_4$ (LPC-R) was synthesized using the sol-gel method, and its surface was subsequently manipulated by varying the concentration of reductant, specifically $NaBH_4$. Structural characterizations reveal that the surface of LPC-R becomes rough and porous due to the reduction treatment, and oxygen vacancies were generated simultaneously. The as-synthesized catalyst was explored as a bifunctional catalyst for water splitting. The surface-reconstructed LPC-2 exhibits enhanced activity for OER and HER, with overpotentials of 260 mV and 104 mV, respectively, and the lower values of Tafel slope. The enhanced electrocatalytic activity of LPC-2 as compared to LPC-R, LPC-1, and LPC-1.5 is attributed to synergistic effects of its morphology, increased charge transfer, oxygen vacancies, enhanced surface area, fast reaction kinetics, and improved conductivity. This work not only provides a strategy for synthesizing defect-rich perovskites but also paves the way for the development of robust and efficient catalysts in the field of energy storage and conversion.

Conflict of Interests

The authors declare no conflict of interest.

Author Contributions

Data curation, Investigation, writing—original draft preparation A.A.; Conceptualization, resources, funding acquisition, M.S.; methodology, funding acquisition, K.G.U.W.; morphological studies, I.K,; All authors have read and agreed to the published version of the manuscript.

Acknowledgements

The Higher Education Commission (HEC) of Pakistan supported this work through grant No. HEC-NRPU 15745 and Commonwealth Split-site Scholarships. AA would like to thank Aryamman Sanyal, Ashley Saunders, and Sandun Dissanayake for their help in XPS, HRTEM, and SEM analysis.

References

1. A. Altaf, M. Sohail, A. Nafady, R. G. Siddique, S. S. A. Shah and T. Najam, *Molecules*, 2023, **28**, 572.
2. N. Tahir, A. Altaf, N. Baig, A. Nafady, A. Ul-Hamid, S. S. A. Shah, P. Tsiakaras and M. Sohail, *Chem. Asian J.*, 2024, e202301100.
3. W. Zeb, A. Altaf, M. Aamir, N. Baig, I. Baig, A. Nafady, M. Sharif, M. Sher and M. Sohail, *J. Saudi Chem. Soc.*, 2022, **26**, 101542.
4. J. Yu, X. Wu, D. Guan, Z. Hu, S.-C. Weng, H. Sun, Y. Song, R. Ran, W. Zhou and M. Ni, *Chem. Mater.*, 2020, **32**, 4509-4517.
5. J. Hwang, R. R. Rao, L. Giordano, Y. Katayama, Y. Yu and Y. Shao-Horn, *Science*, 2017, **358**, 751-756.
6. Y. Zhu, W. Zhou, J. Yu, Y. Chen, M. Liu and Z. Shao, *Chem. Mater.*, 2016, **28**, 1691-1697.
7. R. Zong, Y. Fang, C. Zhu, X. Zhang, L. Wu, X. Hou, Y. Tao and J. Shao, *ACS Appl. Mater. Interfaces*, 2021, **13**, 42852-42860.
8. G. Chen, W. Zhou, D. Guan, J. Sunarso, Y. Zhu, X. Hu, W. Zhang and Z. Shao, *Sci. Adv.*, 2017, **3**, e1603206.
9. K. Lam, Y. Gao, J. Wang and F. Ciucci, *Electrochim. Acta*, 2017, **244**, 139-145.
10. J. Zhang, Y. Ye, B. Wei, F. Hu, L. Sui, H. Xiao, L. Gui, J. Sun, B. He and L. Zhao, *Appl. Catal. B: Environ.*, 2023, **330**, 122661.
11. N. Tsvetkov, Q. Lu, L. Sun, E. J. Crumlin and B. Yildiz, *Nat. Mater.*, 2016, **15**, 1010-1016.
12. Y. Zhang, R. S. Rawat and H. J. Fan, *Small Methods*, 2017, **1**, 1700164.
13. Y. Guo, Y. Tong, P. Chen, K. Xu, J. Zhao, Y. Lin, W. Chu, Z. Peng, C. Wu and Y. Xie, *Adv. Mater.*, 2015, **27**, 5989-5994.
14. R. Shannon, *Acta Cryst. E*, 1976, **32**, 751-767.
15. M. Bilal, A. Altaf, N. Baig, G. A. Chotana, R. S. Ashraf, S. Rasul, A. Nafady, A. Ul-Hamid and M. Sohail, *Fuel*, 2022, **323**, 124324.
16. A. K. Figen and S. Pişkin, *Bull. Mater. Sci.*, 2012, **35**, 203-209.
17. X. Du, M. Chen, S. Shen, P. Zhou, K. H. Lo and H. Pan, *Mater. Today Energy*, 2022, **27**, 101046.
18. C. Zhao, N. Li, R. Zhang, Z. Zhu, J. Lin, K. Zhang and C. Zhao, *ACS Appl. Mater. Interfaces*, 2019, **11**, 47858-47867.
19. G. Zhang, M. Liu, G. Fan, L. Zheng and F. Li, *ACS Appl. Mater. Interfaces*, 2022, **14**, 2768-2781.
20. H. Younan, S. Yue, L. Kai, W. J. Yuan, C. Y. Shen, C. Yixin, F. Chao and L. Xiaomin, 2016.
21. A. Altaf, M. Sohail, M. Altaf, A. Nafady, M. Sher and M. A. Wahab, *Chem. Asian J.*, 2023, e202300870.
22. S.-F. Weng, Y.-H. Wang and C.-S. Lee, *Appl. Catal. B: Environ.*, 2013, **134**, 359-366.
23. P. Van Der Heide, *Surface and Interface Analysis*, 2002, **33**, 414-425.
24. W.-Y. Lee, H. J. Yun and J.-W. Yoon, *J. Alloys Compd.*, 2014, **583**, 320-324.
25. S. Yamamoto, H. Bluhm, K. Andersson, G. Ketteler, H. Ogasawara, M. Salmeron and A. Nilsson, *J. Phys.: Condens. Matter*, 2008, **20**, 184025.
26. C.-F. Chen, G. King, R. M. Dickerson, P. A. Papin, S. Gupta, W. R. Kellogg and G. Wu, *Nano Energy*, 2015, **13**, 423-432.
27. J. Du, T. Zhang, F. Cheng, W. Chu, Z. Wu and J. Chen, *Inorg. Chem.*, 2014, **53**, 9106-9114.
28. J. Suntivich, K. J. May, H. A. Gasteiger, J. B. Goodenough and Y. Shao-Horn, *Science*, 2011, **334**, 1383-1385.
29. D. Friebel, M. W. Louie, M. Bajdich, K. E. Sanwald, Y. Cai, A. M. Wise, M.-J. Cheng, D. Sokaras, T.-C. Weng and R. Alonso-Mori, *J. Am. Chem. Soc.*, 2015, **137**, 1305-1313.
30. X. Gao, H. Zhang, Q. Li, X. Yu, Z. Hong, X. Zhang, C. Liang and Z. Lin, *Angew. Chem. Int. Ed.*, 2016, **55**, 6290-6294.
31. Y. Zhu, W. Zhou, Y. Zhong, Y. Bu, X. Chen, Q. Zhong, M. Liu and Z. Shao, *Adv. Energy Mater.*, 2017, **7**, 1602122.
32. D. den Boer and D. G. Hetterscheid, *J. Am. Chem. Soc.*, 2023, **145**, 23057-23067.
33. M. Bilal, A. Altaf, B.-E. Ehmen, H. K. Zafar, N. Tahir, A. Nafady, M. A. Wahab, S. S. A. Shah, T. Najam and M. Sohail, *RSC Adv.*, 2023, **13**, 23547-23557.
34. M. T. Nguyen Dinh, C. C. Nguyen, N. H. Thi Phan, H. D. Nguyen Phuc, Q. Van Le, S. Y. Kim and L. Nguyen-Dinh, *Ind. Eng. Chem. Res.*, 2023, **62**, 6908-6919.
35. J.-G. Wang, W. Hua, M. Li, H. Liu, M. Shao and B. Wei, *ACS Appl. Mater. Interfaces*, 2018, **10**, 41237-41245.
36. D. Ghosh and D. Pradhan, *Langmuir*, 2023, **39**, 3358-3370.
37. S. Peng, F. Gong, L. Li, D. Yu, D. Ji, T. Zhang, Z. Hu, Z. Zhang, S. Chou and Y. Du, *J. Am. Chem. Soc.*, 2018, **140**, 13644-13653.
38. X. Lü, A. Chen, Y. Luo, P. Lu, Y. Dai, E. Enriquez, P. Dowden, H. Xu, P. G. Kotula and A. K. Azad, *Nano Lett.*, 2016, **16**, 5751-5755.
39. H. Yuan, S. Wang, Z. Ma, M. Kundu, B. Tang, J. Li and X. Wang, *Chem. Eng. J.*, 2021, **404**, 126474.



https://dspace.org/

Surface reconstruction of La0.95Pr1.05CuO4 as an efficient bifunctional electrocatalyst for water splitting

Altaf, Amna; Sohail, Manzar; Wijayantha, Upul K. G.; Kraev, Igor

2026-12-28
Royal Society of Chemistry (RSC)
https://doi.org/10.1039/d5nr03432a
Altaf A, Sohail M, Wijayantha KGU, Kraev I. (2025) Surface reconstruction of La0.95Pr1.05CuO4 as an efficient bifunctional electrocatalyst for water splitting. Nanoscale, Volume 17, Issue 48, December 2025, pp. 27995-28005

Downloaded from a DSpace repository. https://dspace.org/